

8

Recent Trends for the Design and Optimization of Thermoelectric Materials — A Theoretical Perspective

John S. Tse
University of Saskatchewan

Dennis D. Klug
Steacie Institute for Molecular Science

8.1	Introduction	8-1
8.2	Fundamentals of Band Theory and Thermoelectrics	8-2
8.3	Transport Theory Methods	8-4
8.4	Phonon Glasses	8-6
	Glass-like Thermal Conductivity • The Semiconductor Clathrates • Skutterudites • Single and Multiple Band Model	
8.5	New Materials	8-16
	Layered Cobalt Oxides • Quantum Wells and Quantum Wires • Complex Chalcogenides	
8.6	Concluding Remarks	8-24

8.1 Introduction

The application of recent advances in theoretical and computational methods will undoubtedly play a significant role in the design of new materials. This is especially true for materials such as highly efficient thermoelectrics. Even though thermoelectric effects were discovered almost two centuries ago, there remain major challenges to increasing the efficiency of thermoelectric devices. The basic challenge in the development of new thermoelectric materials is to maximize the thermoelectric figure-of-merit, $ZT = \sigma S^2 T / \kappa$, where σ is the electrical conductivity, κ is the thermal conductivity, and S is the Seebeck coefficient or thermopower. This dimensionless quantity provides a measure of the efficiency or performance of a thermoelectric material. Since the optimization of the Seebeck coefficient for any material will involve the appropriate modification of its electronic properties, a fundamental understanding of the electronic band structure will be a valuable, if not essential requirement if the current upper limit of ZT is to be increased significantly. The optimization of the figure-of-merit appears to be a challenging problem since the three properties that determine this quantity are closely connected.

For example, the ratio σ/κ is limited by the ability to reduce the thermal conductivity κ to its limiting value by reducing the contribution from lattice thermal conductivity to a minimum. The remaining contribution to the thermal conductivity is electronic and this is approximately related to the electrical conductivity σ by the Wiedemann–Franz law. The Seebeck coefficient is also partially determined by the electrical conductivity. The objective therefore of theoretical studies is to find ways, in principle, to optimize the figure-of-merit by suggesting materials with optimized electronic band structures and thermal transport properties. There is no well-defined theoretical limit to the figure-of-merit and this provides a challenge for theoreticians and experimentalists alike to search for ways to increase its value. It has been pointed out¹ that a thermoelectric material needs to have $ZT \approx 4$ in order for it to be competitive with a conventional compressor-based refrigeration system. This is not an absolute requirement, however, since even small improvements in materials properties will lead to new applications.

In this review, a selected number of recent developments will be described with emphasis on advances that have been reported since the last review of theoretical techniques was presented in this series in 2001.² A main focus is to present recent experimental and theoretical progress in the “resonant scattering” mechanism which forms the basis of the phonon glass assumption and the application of the concept of *phonon glass electron crystal* (PGEC) on the design of new thermoelectric materials, particularly the clathrates and skutterudites. We also comment on the recent and very promising development of NaCoO₂. Finally, the potential of chalcogenide complexes and nanostructured materials will be reviewed briefly.

8.2 Fundamentals of Band Theory and Thermoelectrics

The calculation of thermoelectric properties from first principles employs modern band structure theory methods² that take advantage of new computational methods as well as advances in computer technology. The primary method for band structure calculations is that of density functional theory (DFT). There are many excellent reviews and textbooks on electronic structure methods³; therefore, only a brief summary is given here. This method is based on the Hohenberg–Kohn (HK) theorem^{4,5} that may be summarized as follows:

The ground state energy of a system of interacting electrons is a unique functional of the charge density. For a system with fixed number of electrons, the functional has its minimum value for the correct ground state energy for variations in the charge density.

The theorem was initially proven for a nondegenerate ground state but recent work has extended it to arbitrary ground state. In essence, the ground state energy functional $E[n]$ for an N -electron system under an external field V_{ext} is represented as

$$E[n] = F[n] + \int V_{\text{ext}}(\vec{r})n(\vec{r})d\vec{r} \quad (8.1)$$

The undefined functional $F[n]$ is a function of the electron density $n(r)$, and includes all the kinetic energy and electron–electron interactions term. After subtracting out the Coulomb contribution, the remaining functional $G[n]$ accounts for the exchange and correlation effects of the electron–electron interactions:

$$G[n] = F[n] - \int \frac{n(\vec{r})n(\vec{r}')}{|\vec{r} - \vec{r}'|} d\vec{r}d\vec{r}' \quad (8.2)$$

According to the HK theorem⁴ the variational equation for the ground state energy subject to the constraint of fixed number of electrons is

$$\delta\{E[n]\} - \mu \int n(\vec{r})d\vec{r} = 0 \quad (8.3)$$

Approximating the kinetic functional with noninteracting kinetic energy operators:

$$T[n] = -\frac{1}{2} \sum_i \nabla_i^2 \quad (8.4)$$

and assuming a one-electron orbital basis set, the ground state energy of the interacting electron system is given by the following Kohn–Sham equation⁵:

$$E[n] = \sum_i^N \int \varphi_i^*(\vec{r}) \left(-\frac{1}{2} \nabla_i^2 \right) \varphi_i(\vec{r}) d\vec{r} + \int V_{\text{ext}}(\vec{r}) n(\vec{r}) d\vec{r} + \iint \frac{n(\vec{r})n(\vec{r}')}{|\vec{r} - \vec{r}'|} d\vec{r} d\vec{r}' + E_{\text{xc}}[n] \quad (8.5)$$

The explicit form of the exchange–correlation functional $E_{\text{xc}}[n]$ is unknown. To a first approximation, $E_{\text{xc}}[n]$ can be assumed to be the exchange correlation energy $\varepsilon_{\text{xc}}[n]$ for an interacting electron gas of uniform density:

$$E_{\text{xc}}[n] = \int \varepsilon_{\text{xc}}[n(\vec{r})] n(\vec{r}) d\vec{r} \quad (8.6)$$

This is known as the *local density approximation* (LDA). It is assumed that the density locally can be treated as a uniform electron gas, or equivalently that the density is a slowly varying function. The functional forms of $\varepsilon_{\text{xc}}[n]$ have been treated by many authors and is still a subject of intense research.

It is obvious that improvement over the LDA approximation will have to consider a nonuniform electron gas. A step in this direction is to make the exchange and correlation energies dependent not only on the electron density, but also on the derivatives of the density. Such methods are known as *generalized gradient approximation* (GGA).⁶ A popular GGA function used in many solid-state calculations was proposed by Perdew and Wang.⁷ For the correlation energy, several gradient corrected functionals have been proposed. A proposal due to Lee, Yang, and Parr (LYP)⁸ was often employed. In comparison with HF theory, DFT eliminates the numerical effort in the computation of the elements of the exchange integral matrix K . Furthermore, the effective potential $V_{\text{eff}}(r)$ is common to all the one-electron Schrödinger equations.

Highly accurate numerical methods, such as the full potential linearized augmented plane-wave (LAPW)⁹ and linear combination of muffin tin orbitals (LMTO)¹⁰ have been developed to solve the all-electron Schrödinger equation. In both approaches, the system is partitioned into atomic regions and an interstitial region. Formally the two methods are equivalent and should produce the same results. In the atomic region, electronic wave functions are easily obtained from solving atomic-like Schrödinger equations. The most significant difference between the two methods is in the treatment of the interstitial region. In the LAPW method, a plane-wave expansion is used to describe the wave function in the interstitial region while the LMTO method employs a basis set of spherical Bessel and Hankel functions. Theoretical and technical details of the two methods can be found in several textbooks and review articles^{9,10} and, therefore, will not be presented here.

The atom-centered (localized) basis set is very good in describing atom core orbitals. If the atomic core contributions to the external potential can be replaced by a pseudopotential, a more flexible basis set based on plane-waves can be used to describe the valence electrons. The plane-wave basis set is particularly efficient for electronic calculations of periodic system. Applying Bloch's theorem, the wave function is the product of a periodic part and a wave-like part¹¹:

$$\varphi_i(\vec{r}) = \exp(i\vec{k}\vec{r}) \sum_{\vec{G}} c_{i,\vec{G}} \exp(i\vec{G}\vec{r}) = \sum_{\vec{G}} c_{i,\vec{k}+\vec{G}} \exp[i(\vec{k} + \vec{G})\vec{r}] \quad (8.7)$$

The *completeness* of the basis set expansion can be easily controlled by adjusting the value of the energy cutoff defined by

$$\frac{\hbar^2}{2m} |\vec{k} + \vec{G}|^2$$

Substituting the plane-wave basis set into the Kohn–Sham equation gives a particularly simple form:

$$\sum_{G'} \{H_{k+G, k+G'}\} c_{i, k+G'} = \varepsilon_i c_{i, k+G'} \quad (8.8)$$

$$H_{k+G, k+G'} = |\vec{k} + \vec{G}|^2 \delta_{GG'} + V_{nn}(\vec{G} - \vec{G}') + V_{elec}(\vec{G} - \vec{G}') + V_{xc}(\vec{G} - \vec{G}')$$

where

$$V_{elec} = - \int \frac{n(\vec{r})}{|\vec{r} - \vec{r}'|} d\vec{r} \quad (8.9)$$

In this form, the reciprocal space representation of the kinetic energy (first term) is diagonal and the various potential terms can be described in terms of their Fourier components.

The Hamiltonian matrix can be solved by the conventional diagonalization method. Depending on the energy cutoff of the plane-wave expansion, this task can be quite demanding. One of the most important information obtain from a band structure calculation is the energy dispersion of the electronic bands (electronic band structure). As will be shown in the next section, this information is required for the calculation of the electronic transport properties.

The DFT method is becoming the *de facto* computational technique for condensed matters. The method often provides accurate electronic band structures for a wide range of materials. As will be discussed below, for highly correlated systems, such as the transition metal oxides, additional approximations are needed to correct some deficiencies of the method. It is noteworthy that extreme caution must be exercised when applying the method to heavily “doped” polymers. Recent calculations have shown that the LDA and GGA approximation fail to describe correctly the formation of polaron or bipolaron states. For the study of the electronic structure of these materials, the Hartree–Fock or hybrid functional (mixing Hartree exchange with density functionals) must be used.

8.3 Transport Theory Methods

Transport properties relevant to thermoelectric materials, such as the Seebeck coefficient and the Hall coefficient, can be calculated from the electronic band structures and with standard kinetic theory provided that the electronic relaxation time $\tau(E)$ is known. Fortunately, in most cases $\tau(E)$ does not vary significantly with the energy E at low temperature and can be approximated by a constant value, i.e., isotropic relaxation time approximation. It has been found that, using this isotropic relaxation time approximation, reasonably accurate results can be obtained.

Transport properties can be estimated using standard kinetic theory described in detail in textbooks such as that of Ziman.¹² In the low-field limit the electrical conductivity of a crystalline metallic solid can be calculated from its band structure by the energy integral:

$$\sigma_0(T) = \frac{e^2}{3\hbar} \int dE \tau(E) N(E) v^2(E) \left[- \frac{\partial f(E)}{\partial E} \right] \quad (8.10)$$

where e , τ , f , and v are the electron charge, electronic relaxation time, Fermi distribution function, and Fermi velocity, respectively. The Seebeck coefficient is proportional to the electron velocity and the electron density of states convoluted by the Fermi distribution function and can be calculated from the

ratio of the 0th and 1st moment of the electrical conductivity:

$$S(T) = \frac{1}{eT} \frac{I^1}{I^0} \quad (8.11)$$

where

$$I^x(T) = \int dE \tau(E, T) N(E) v^2(E) (E - E_F)^x \left[-\frac{\partial f(E)}{\partial E} \right] \quad (8.12)$$

The Hall concentration is given by

$$n_H = -\sigma^2 / e\sigma_H \quad (8.13)$$

$$\sigma_H = \frac{e^3}{6\hbar} \int dE \tau^2(E, T) N(E) \tilde{v}(E) [\text{Tr}(\tilde{M}^{-1}) - \tilde{M}^{-1}] \tilde{v}(E) \left[-\frac{\partial f(E)}{\partial E} \right] \quad (8.14)$$

where \tilde{M}^{-1} represents the inverse mass tensor.

It is clear from the equations for the Seebeck coefficient that an ideal thermoelectric material will have a high electronic density of states near the Fermi level and a reasonable electrical conductivity that would be determined by nearby dispersive electronic bands. Figure 8.1 shows schematically the requirements for an efficient thermoelectric material.

There are several similar schemes reported in the literature for the evaluation of the Fermi surface integrals 8.12 and 8.14.^{13–15} These include the use of a very dense k -point mesh with the modified Shankland–Koelling–Wood (SKW) band interpolation scheme¹⁴ that uses a simple filtering technique to suppress high-frequency oscillations in interpolated band structures. An alternative method employs evaluation of intraband optical matrix elements.¹⁵ These matrix elements can be obtained in optical properties codes that are part of full-potential linear augmented plane-wave codes such as WIEN2k.¹⁶ A large number of k points in the first Brillouin zone are required for these calculations to obtain sufficient accuracies.

To treat doping in semiconductor thermoelectric materials, the simplest approach often employed is the rigid band approximation.^{13,15,17} In this approach, it is assumed that the band structure is unchanged by the doping and that n- and p-doping are simulated by moving the Fermi level for the calculation of the Seebeck coefficient. This approach is assumed to be suitable for low doping levels but testing is required for each material or class of material.

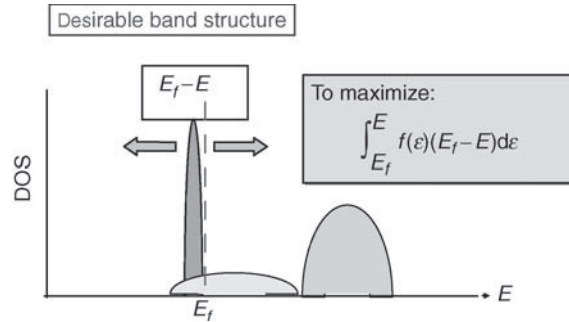


FIGURE 8.1 A schematic diagram showing the most favorable electron density of states for a potential high efficiency thermoelectric material. The broad band corresponds to a parabolic electronic band for carrier (electron or hole) transport and the narrow band near the Fermi level helps to enhance the Seebeck coefficient.

8.4 Phonon Glasses

8.4.1 Glass-like Thermal Conductivity

In this section we discuss one of the classes of materials that have a very high potential for thermoelectric applications. These materials are the PGEs.¹⁸ These classes of materials are crystalline that possess “glass-like” thermal conductivity. That is, these materials have lattice thermal conductivities similar to amorphous materials but have electronic structures that can be described as for crystalline solids. Since the electronic properties are believed to be accessible to modification in this material, it is believed that they are excellent candidates for efficient thermoelectrics.

The basic ideas describing the thermal conductivity of crystal with glass-like behavior were developed by R.O. Pohl and his collaborators¹⁹ almost two decades ago. It was, however, concluded at that time that the many aspects of the thermal transport properties in glasses and the physical origin of the low thermal conductivity were not well understood. Basically, the low thermal conductivity in an amorphous solid is due to the small phonon mean-free paths that can arise from damped localized oscillators rather than the normal phonons in a crystalline lattice. The goal for a suitable thermoelectric material therefore is to maintain high electrical conductivity while at the same time having the thermal conductivity of an amorphous solid. Significant progress has been made in the last decade towards an understanding of the nature of the low thermal conductivity in phonon glasses. In particular, the electronic band structures of many potential thermoelectric have been calculated and analyzed.²⁰ In this section we review research in this area with emphasis on work done in our laboratory.

There are several ways to effectively reduce the thermal conductivity and at the same time maintain or optimize the electronic structure of a material. Compounds that have been considered are the silicon clathrates and their analogues.²¹ A clathrate is a compound consisting of a cage-like structure that encloses guest molecules or atoms. As an example, there are basically two clathrate structures made from silicon or germanium. These are analogues of the well-known clathrate hydrate compounds²² that exist in nature or can be made in the laboratory. The two structures are illustrated in Figure 8.2. The type I clathrate has a cubic crystal structure and has an ideal stoichiometric ratio of cage atom or molecules to cage molecules in the case of the clathrate hydrate of 46 to 8, assuming both the large and small cages are completely filled (see Figure 8.3). The type II clathrate is also cubic but with a cage-to-guest ratio of 136 to 24 assuming all cages are filled. A typical guest in the silicon clathrate is an alkali metal atom. Experimental and theoretical studies of the stabilities, electronic structures,^{23–26} and vibrational properties of pure and doped silicon and related clathrate compounds have been reported. A particularly important type I clathrate found in nature in vast quantities is the methane clathrate hydrate. In addition to having the same crystal structure as some of the silicon clathrates, it provides an excellent material for testing theories of the thermal conductivity for clathrates in general.

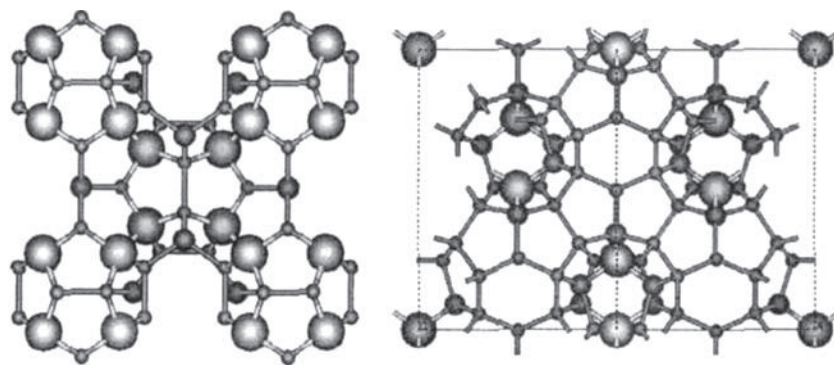


FIGURE 8.2 The cubic clathrate structures (left) type I clathrate with 46 Si atoms per unit cell and (right) type II clathrates with 136 atoms per unit cell.

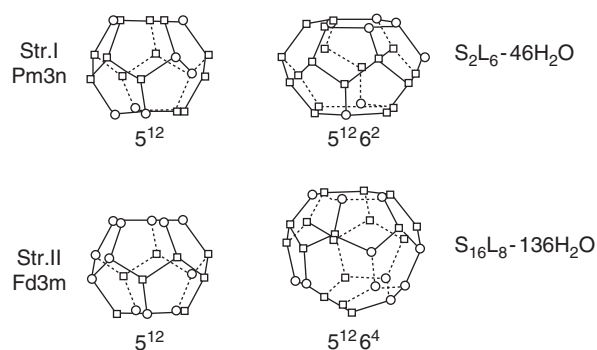


FIGURE 8.3 The cages forming the type I and type II clathrates.

A scheme for the glass-like thermal conductivity of the clathrates has been proposed.²⁷ It was suggested that there needs to be localized vibrations within the frequency range of the acoustic phonon branches and that clathrates with heavy guest atoms and light framework elements were desirable for optimum thermoelectric properties. This study also reported thermal conductivity data for the Na_8Si_{46} clathrate and showed that it was the same as in an amorphous solid. It was postulated that the low thermal conductivity of the metal-doped semiconductor clathrate compounds is due to resonant scattering of lattice phonons by the localized vibrations of the dopants.²⁸ Resonant scattering occurs due to “avoided crossing” interactions of phonon modes with the localized vibrations of the guest atoms²⁹ (see Figure 8.4).

The thermal conductivities of several clathrate compounds with semiconducting elements forming the lattice framework have been reported.³⁰ Surprisingly, the profile of the thermal conductivity differs significantly from one system to the other. The experimental thermal conductivity for clathrate compounds of Cs_8Sn_{44} , $Ba_6Ga_{16}Si_{30}$, $Sr_6Ga_{16}Ge_3$, $Eu_8Ga_{16}Ge_{30}$, $Eu_8Ga_{16}Ge_{30}$, and $Sr_4Eu_4Ga_{16}Ge_{30}$ are shown in Figure 8.5. It is interesting to note that only $Sr_4Eu_4Ga_{16}Ge_{30}$ clearly shows glass-like thermal conductivity behavior. At the other extreme, the “simple” Cs_8Sn_{44} behaves like a normal crystalline solid. $Ba_6Ga_{16}Si_{30}$ show a thermal conductivity profile resembling that of resonant scattering by impurities. The remaining compounds, while showing a glass-like thermal behavior at high temperatures (>30 K),

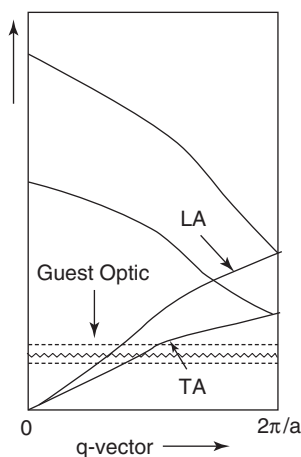


FIGURE 8.4 A schematic representation of “avoid crossing” between the localized vibrations of the guests with the clathrate framework acoustic phonon branches.

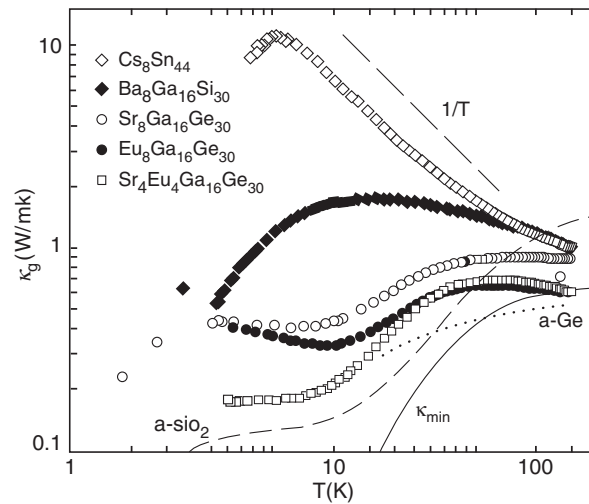


FIGURE 8.5 Experimental thermal conductivity for type I clathrate of $\text{Cs}_8\text{Sn}_{44}$, $\text{Ba}_8\text{Ga}_{16}\text{Si}_{30}$, $\text{Sr}_6\text{Ga}_{16}\text{Ge}_{30}$, $\text{Eu}_6\text{Ga}_{16}\text{Ge}_{30}$, and $\text{Sr}_4\text{Eu}_4\text{Ga}_{16}\text{Ge}_{30}$. Note the very different temperature profiles between the clathrates.

the thermal conductivity actually increases at lower temperature. Therefore, the simple picture of heat-carrying phonon scattering due to the rattling motions of the “guests” needs to be examined in detail.

Theoretical phonon band structures together with experimental data for thermal conductivity of $\text{Na}_8\text{Si}_{46}$ and $\text{Cs}_8\text{Sn}_{46}$ were analyzed.³¹ The conclusion was that the glass-like thermal conductivity in $\text{Na}_8\text{Si}_{46}$ is due to the scattering of thermal phonons due to *avoided crossing* of localized phonon bands of the metal with the framework transverse acoustic (TA) branch of the same symmetry in the framework. In contrast, for $\text{Cs}_8\text{Sn}_{46}$ significant hybridization of the vibrations of the Cs atoms and the lattice modes was found. Therefore, the Cs vibrations mixed with the lattice modes and can no longer be considered as localized oscillators. As a result there is no “resonant scattering” in this system and it is reflected in the normal crystalline-like thermal conductivity observed experimentally. It was emphasized that dopant metal atoms had to be carefully selected in order not to be too light, such that their vibrations in the clathrate cages were at higher frequencies than the maximum of the TA branch or too heavy such that resonant phonon scattering would be prohibited.

Direct experimental evidence of *avoided crossing* in clathrates was obtained on a study of the methane and xenon clathrate hydrates using the technique of very high energy resolution inelastic x-ray scattering (IXS) and comparing these results with inelastic neutron scattering (INS) and lattice dynamics calculations.³² In this study, the low-frequency dispersion curves were measured and clear evidence for avoided crossings between the acoustic phonons and localized guest modes was observed. This is consistent with the resonant scattering model³³ where a mixing of acoustic lattice phonons and localized guest modes of the same symmetry occurs with a resulting exchange of energy. Lattice dynamics calculations on clathrate structures with high-quality interaction potentials supported this avoided crossing picture and the results for the methane and xenon clathrate dispersion curves are shown in [Figure 8.6](#) and [Figure 8.7](#). The anticrossing behavior in these clathrates is illustrated by the strong bending of the longitudinal and transverse acoustic branches of the host phonons at the crossing points with those of the guests. The calculated dispersion relationship for a polycrystalline methane hydrate from IXS is shown in [Figure 8.8](#). The theoretical prediction was substantiated by the IXS experiment reported in a recent paper.³⁴ This study therefore yielded strong support to the suggestion of the resonant scattering model for the origin of the low thermal conductivity in the clathrates.

In passing, it is important to mention that a recent measurement of the thermal conductivity of an “empty” structure II Si clathrate has also shown a glassy-like behavior. This observation apparently

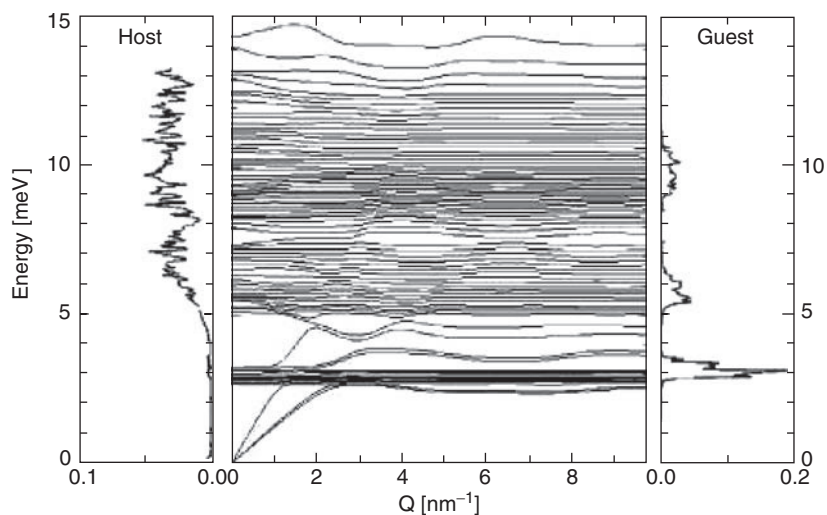


FIGURE 8.6 Calculated powder averaged dispersion curves for the methane clathrate. The characteristic vibrations of the guest methane molecules are at 3, 5, and 9 meV. The density of vibrational states of the host and guest molecules are shown on the left and right sides of the phonon dispersion curves, respectively.

contradicts the “resonant scattering” mechanism. The experiment by itself that indicates a glassy thermal behavior of a crystalline material with no low-frequency localized vibration is surprising and contrary to our current understanding of thermal conduction in condensed matter. It is known, however, that the synthesis of a “pure” empty Si clathrate is very difficult. Further experimental studies are needed to determine the nature of the sample which can shed new light on this perplexing problem.

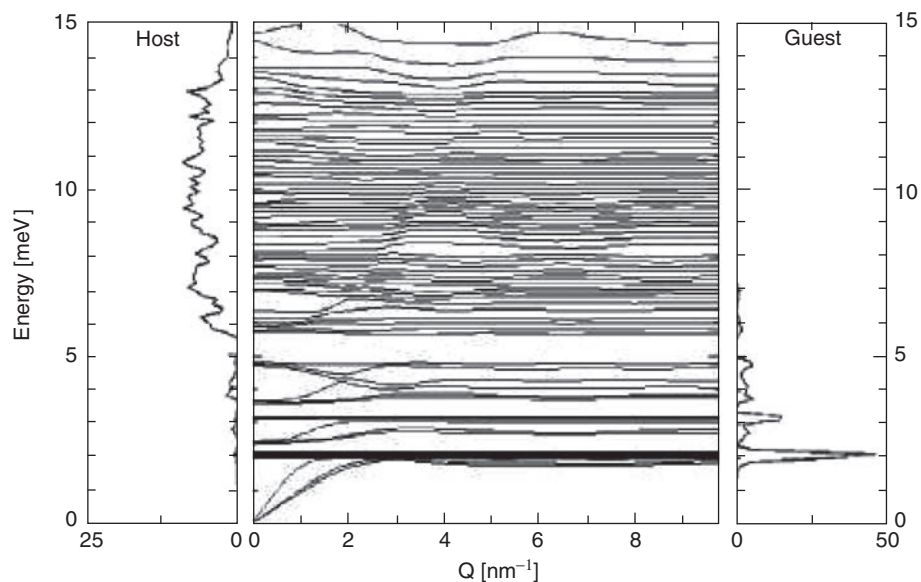


FIGURE 8.7 Calculated powder averaged phonon dispersion curves for the xenon hydrate. The density of vibrational states of the host and guest molecules are shown on the left and right sides of the phonon dispersion curves, respectively. The characteristic vibrations of the xenon atoms are at 2, 3, and 4 meV.

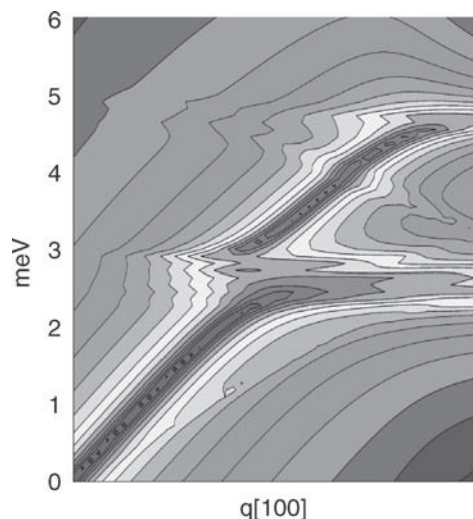


FIGURE 8.8 (See color insert following page 31-12.) Calculated longitudinal phonon dispersion curve for polycrystalline type I methane hydrate. The avoided crossing is clearly shown.

Fundamental questions are how and why the clathrate structures are stabilized with respect to crystalline Si and the role of the Na dopant on the phase stability. In both elemental Si and the clathrates, each Si atom is bonded to four nearest neighbors. The difference between these structures is the way that these tetrahedra are packed and the dependence of the packing upon the valence electron concentration. The Si atoms in elemental Si are part of the six-member rings, whereas both five- and six-member rings are found in the clathrate structures.³⁵ Thus, it is important to understand the phase stability and its relationship to the structure. To explore this issue, the electronic structures are analyzed with the method of moments augmented with the second moment scaled tight-binding Hamiltonian.³⁶ This approach offers the advantage that one may decompose the results into structurally meaningful quantities in a much simpler way than in first principles methods and thus is ideal for a *qualitative* analysis of the dependence of phase stability upon electron concentration.³⁶ The ensuing discussion will assume complete charge transfer from Na and a rigid band model where only the Si atoms are considered. With this assumption the effective valence electron count for crystalline Si is $4e/\text{Si}$ and for the type I $\text{Na}_8\text{Si}_{46}$ it is $4.17e/\text{Si}$, whereas for the type II $\text{Na}_x\text{Si}_{136}$, which exhibits a wide range of stoichiometries, it is between $4.0e/\text{Si}$ ($x = 0$) and $4.18e/\text{Si}$ ($x = 24$). Figure 8.9a shows the total energy differences, obtained from tight-binding calculations,³⁷ between the Si framework of the clathrates and that of elemental Si as a function of the number of valence electrons. The Si diamond lattice is most stable at effective electron counts from $4.0e/\text{Si}$ to $4.4e/\text{Si}$, while the next most stable structure is type II $\text{Na}_{24}\text{Si}_{136}$, then followed by the type I $\text{Na}_8\text{Si}_{46}$ structure which becomes the most stable structure above $4.4e/\text{Si}$. The shape of these energy difference curves can be fully understood in terms of the moments (μ_n) of the density of states (DOS). In general, the number of nodes (including the two end points) in these curves is equal to the moment which is most responsible for the energy difference between the two structures. Within a tight-binding description these moments are theoretically connected to local structural features and thus may be used to relate the structural topology to the total electronic energy.³⁶ The energy difference curves can be reconstructed by expanding the DOS in terms of contributions from the various moments via a continued fraction expansion, which may be truncated at any given moment. It is clear from Figure 8.9a that the energy difference curves between the clathrate structures and Si contain exactly five nodes, indicating a strong m_5 component which is related to the number of five-member rings which provide stability just above the half-filled band.³⁶ Since there are more five-member rings per Si in the $\text{Na}_{24}\text{Si}_{136}$ structure, it is more stable than $\text{Na}_8\text{Si}_{46}$. Thus the reconstructed DOS of Figure 8.9b which contains

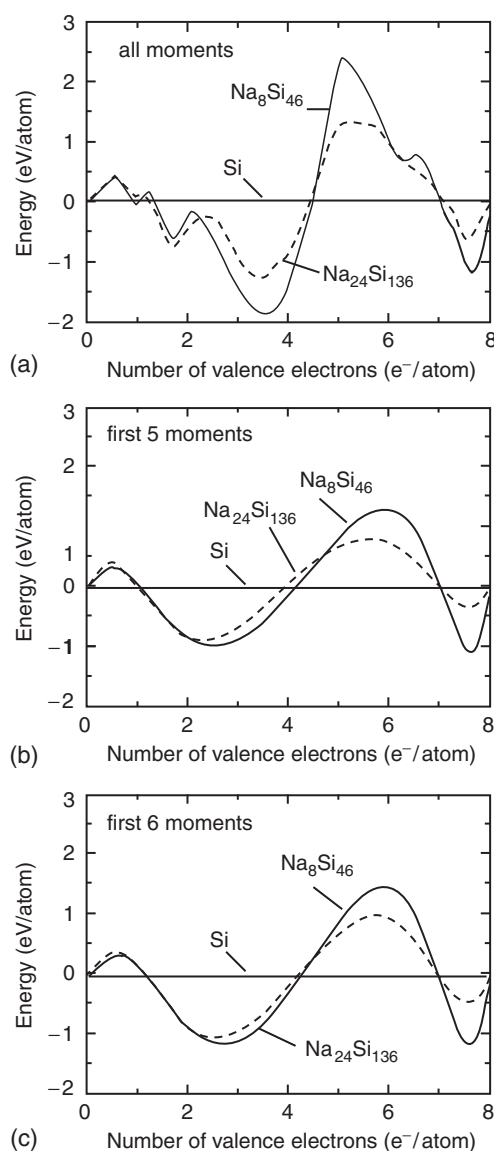


FIGURE 8.9 Energy difference curves for elemental Si, type I Na₈Si₄₆ and type II Na₂₄Si₁₃₆. The convention of these curves is that the structure with the highest energy is most stable at that electron count. (a) All moments; (b) up to fifth moment; and (c) including sixth moment.

only the energy components up to μ_5 is qualitatively correct in terms of phase ordering. Inclusion of μ_6 (Figure 8.9c), which is responsible for stabilizing elemental Si due to the large number of six-member rings in the diamond lattice, improves the agreement with the full calculation but does not qualitatively alter the trend. This simple calculation captures the essence of the important trend that *both* clathrate structures are, in fact, only metastable with respect to disproportionate into Na and Si. The binding energies are estimated to be 0.1–0.2 eV above elemental Si, in agreement with more sophisticated calculations.³⁸ Furthermore, the predicted energetic ordering is also correct in that the Na₂₄Si₁₃₆ structure is only marginally more stable than Na₈Si₄₆. However, the current analysis demonstrates that the clathrate structures are stabilized relative to Si at higher electron counts due to the formation of the

five-member rings in these structures and should also be valid for other clathrate materials based on Ge or Sn. Thus the stability of the clathrates may be enhanced if the effective number of valence electrons on the clathrate framework could be increased. The approach was recently extended in an examination of the structural properties of metal-doped clathrate compounds of C, Si, Ge, and Sn.³⁹ Clathrate-type phases based on the frameworks Si_{172} , Ge_{172} , Si_{40} , and Ge_{40} are not only likely to be energetically favorable but may also exhibit high thermoelectric efficiency.

8.4.2 The Semiconductor Clathrates

The dependence of the Seebeck coefficient on the Na dopant concentration can be investigated by theoretical calculations.⁴⁰ The results for the calculation on both type I and type II Na-doped Si clathrates are shown in Figure 8.10. The calculations show that the larger the Na concentration, the smaller the Seebeck coefficient. At low Na doping, such as $\text{Na}_2\text{Si}_{46}$, $\text{Na}_6\text{Si}_{46}$, and $\text{Na}_8\text{Si}_{136}$, the Seebeck coefficient has a large negative value that results from a delicate balance between electron and hole carriers. The transport properties of a Si clathrate with a nominal composition of $\text{Na}_8\text{Si}_{46}$ have been reported.⁴¹ Results of the measurements are shown in Figure 8.11. In agreement with the theoretical prediction, the thermal conductivity behavior of $\text{Na}_8\text{Si}_{46}$ resembles that of an amorphous solid. It should be noted that, in order to make a direct comparison with the “universal” form for a glass, it is essential to plot the scaled thermal conductivity⁴² (κ/C) against (T/Θ_D) where κ is the thermal conductivity, the scaling factor $C = 4\pi k_B^3 \Theta_D / h^2 v$, k_B is the Boltzmann constant, h is the Planck constant, v the group velocity, and Θ_D is the Debye temperature of the material. The high-temperature thermal conductivity of $\text{Na}_8\text{Si}_{46}$ is an order of magnitude larger than $\text{Ba}_8\text{Ge}_{16}\text{Si}_{30}$ and $\text{Ba}_8\text{Ge}_{16}\text{Ga}_{30}$. This is mainly due to the higher electronic contribution for $\text{Na}_8\text{Si}_{46}$. The large electrical conductivity also lowers the

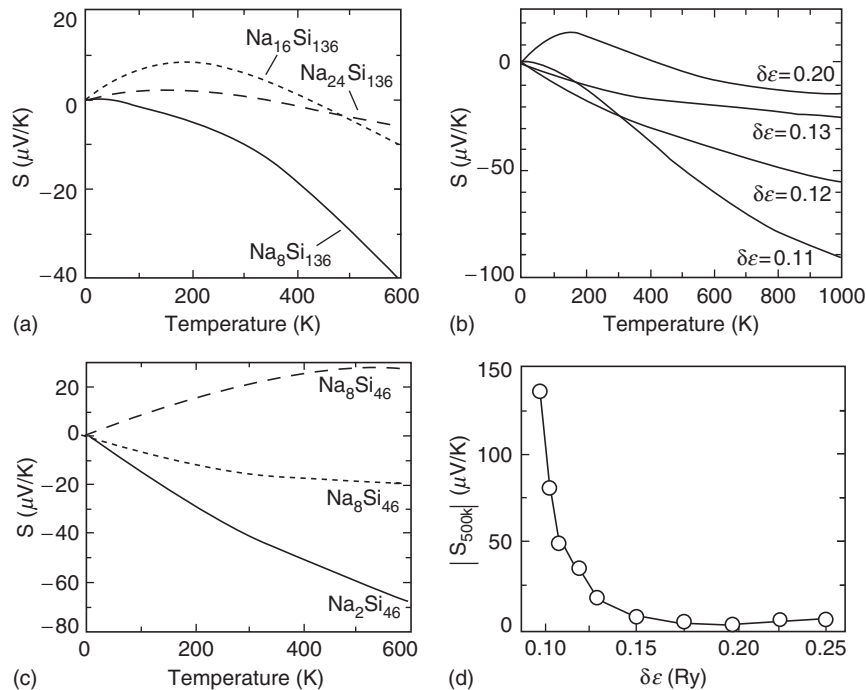


FIGURE 8.10 Calculated Seebeck coefficient S for (c) $\text{Na}_x\text{Si}_{46}$ ($x = 2, 6$, and 8) and for (a) $\text{Na}_x\text{Si}_{136}$ ($x = 8, 16$, and 24). The Seebeck coefficient was obtained under a rigid band approximation. (b) The effect of increasing dopant concentration is simulated by increasing the Fermi level above that found for the neutral cage by an amount $\delta\epsilon$. The value of S as a function of d' at $T = 500$ K is shown in (d).

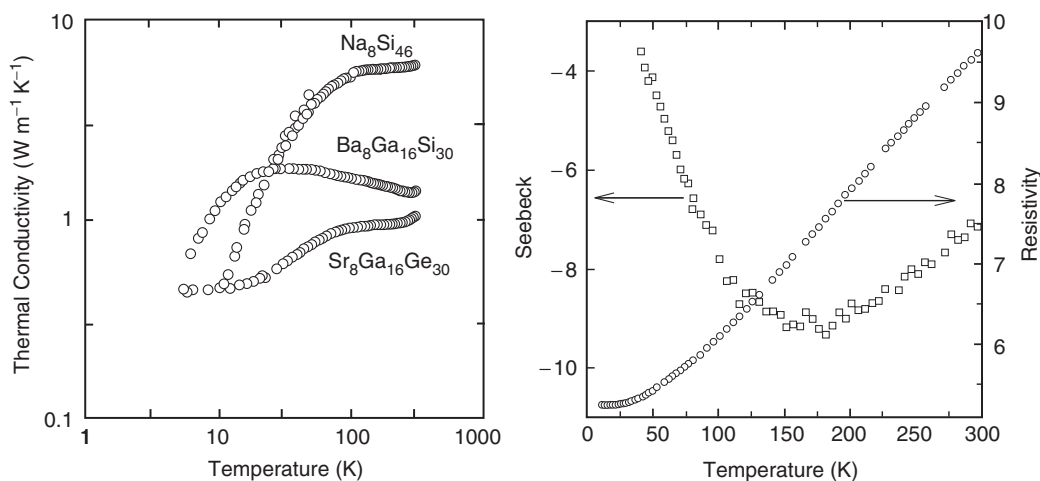


FIGURE 8.11 Experimental thermal conductivity, resistivity, and Seebeck coefficient for $\text{Na}_8\text{Si}_{46}$.

thermopower (S) of this material. In comparison with the theoretical prediction, it is interesting to note that the measured Seebeck coefficient is closer to those calculated for $\text{Na}_6\text{Si}_{46}$. The discrepancies are relatively small and within the accuracy limit of the Boltzmann transport model. The theory, however, suggests that the Seebeck coefficient can be improved substantially by reducing the Na concentration. The general trend is in good agreement with experiments^{43–45} even though the calculated magnitudes are somewhat lower.^{46,47} The calculated overall trend of S as a function of Na concentration may be ascribed to the band profile of the Si framework. Calculations performed on the Si_{46} clathrate, where the conduction bands are occupied simply by raising the Fermi level by an amount $\Delta\epsilon$ qualitatively reproduce the temperature dependence of S (Figure 8.10c) and the important trend that lower concentrations of electropositive atoms lead to larger S . For low Na concentration only the lower energy conduction bands are occupied. These bands are sparse and relatively flat, resembling a semimetal. At higher Na concentration (i.e., higher Fermi level), the conduction bands are more free-electron-like resulting in a low Seebeck coefficient. Thus, lower concentrations of electron donating elements are desirable to maximize S . A lower Na concentration will reduce the electrical conductivity but at the same time decrease the electronic component of the thermal conductivity even though experimentally the control of the stoichiometry of the alkali metal concentration in clathrates is not an easy task.

8.4.3 Skutterudites

Another promising new class of potential high efficiency thermoelectric materials is the skutterudites. The subject has been reviewed in two recent articles.^{48,49} The skutterudites are binary compounds with a composition of MX_3 , where M is a Group 9 transition metal (Co, Rh, and Ir) and X Group 15 nonmetals P, As, and Sb and a body-centered structure. A typical unit cell is shown in Figure 8.12. The metal M atoms are situated at the corners of the unit cell and the nonmetallic X atoms forms square structures occupying six of the eight empty “quadrants.” The remaining two voids can be filled with other metal atoms (guests) just as in the case of the clathrates. The filled skutterudite has a general stoichiometry of $\text{RM}'_x\text{M}_{3-x}\text{X}_{12}$ where R is usually a rare-earth element. The electronic structure of the host lattice can also be changed by replacing the Group 9 atoms (M) with the electron deficient Group 8 atom (M'). These filled skutterudites display a wide range of electronic properties ranging from semiconducting to metallic and even superconducting. For example, depending on the concentration, a filled skutterudite of $\text{Ce}_y\text{Fe}_{4-x}\text{Co}_3\text{Sb}_{12}$ can change from a p-type to an n-type semiconductor. The guests can be chosen to modify the electronic and phonon properties in order to enhance the thermoelectric property. It is noteworthy that a very

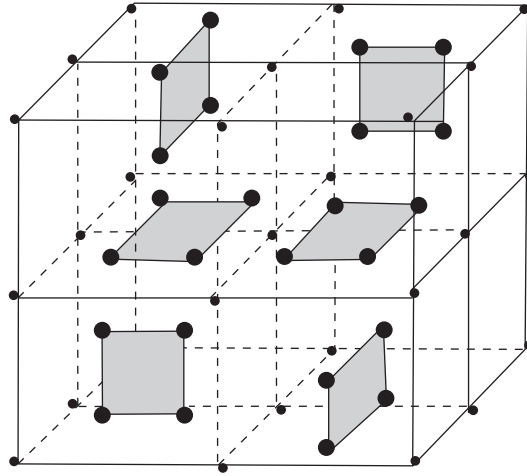


FIGURE 8.12 The skutterudite structure.

interesting relationship between the nature of the “filler” ions with the lattice constant the positional parameters and the size of the voids have been found in various family of filled skutterudites.

It is generally believed that the heavy rare-earth atom serves as the “rattler” and helps to scatter the lattice phonons and reduce the thermal conductivity. The low-frequency vibrational modes have been investigated in $\text{La}_{0.9}\text{Fe}_3\text{CoSb}_{13}$ from heat capacity measurements. It is shown that the “excess” heat capacity at low temperature between the filled skutterudite with pure CoSb_3 can be attributed to two additional localized vibrations (Einstein oscillator) with energy 6 meV (70 K) and 18 meV (200 K). The energy of the localized vibrations are in reasonable agreement with the La localized vibrations of 7 and 15 meV deduced from a comparison of the neutron incoherent inelastic scattering data between $\text{LaFe}_4\text{Sb}_{12}$ and $\text{CeFe}_4\text{Sb}_{12}$.⁵⁰ The experimental results are also consistent with the prediction from a recent *ab initio* lattice dynamics calculation.⁵¹ The temperature profile of the thermal conductivity of filled skutterudites does not show glassy anomaly as in the clathrates.⁴⁸ However, the profile of the thermal conductivity is indicative for materials where phonons are scattered through resonant scattering by impurities as only the low temperature thermal conductivity is reduced substantially. For example, the temperature dependence of the thermal conductivity in double-filling p-type $\text{Ce}_{1-x}\text{Yb}_x\text{Fe}_4\text{Sb}_{12}$ is shown in Figure 8.13.⁵² It is obvious that the thermal conductivity does not change significantly for temperatures higher than 100 K.

The Seebeck coefficients and carrier concentration can be estimated from a simple formula relating the lower edge of the conduction band and the moments of the electron density of a free electron gas. Model calculations on filled CoSb_3 show a very large $S^2\sigma$ value of $16 \times 10^{16} (\mu\text{V})^2/\text{cm}/\text{K}$ ⁵³ and an n-doped effective mass (with Ce) as high as $6m_e$.⁴⁸ Therefore, the combination of low thermal conductivity and large Seebeck coefficient make the skutterudites a strong contender for high efficiency thermoelectric materials. Experimentally, the figure-of-merit, ZT , reaches almost 1.5 at 900 K for p-type CeFeCoSb_{12} and n-type $\text{Ba}_{0.3}\text{Ni}_{0.05}\text{Co}_{3.95}\text{Sb}_{12}$.⁴⁸

8.4.4 Single and Multiple Band Model

There is no obvious theoretical limit for the merit of index, ZT . According to band structure theory for a single metallic electronic band, a simple relationship⁵⁴

$$S = \frac{\pi^2 k^2 T}{3e} \left. \frac{d \ln \sigma(E)}{dE} \right|_{E_F} \quad (8.15)$$

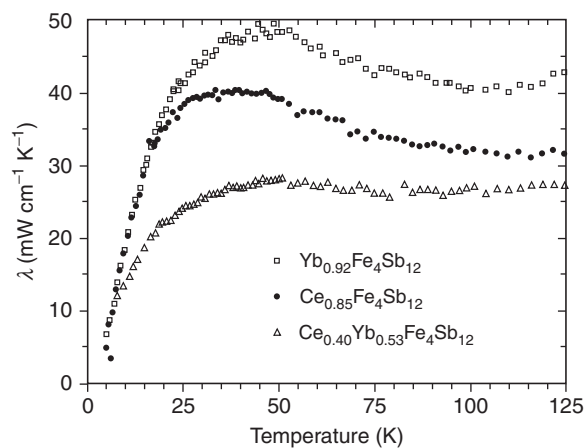


FIGURE 8.13 Experimental thermal conductivity for selected skutterudites.

that relates the thermopower (or Seebeck coefficient) with the electronic DOS $\sigma(E)$ near the Fermi level E_F can be derived. A potential high efficiency thermoelectric material must have a high electron DOS at the Fermi level. Unfortunately, for most materials, the condition of high DOS and also high electrical conductivity cannot be easily met concurrently. For realistic materials, the electronic band structures near the Fermi level are often very complex and the transport properties are not necessarily dominated by a single electronic band. As presented above, apart from low thermal conductivity, a favorable scenario for a potential high thermoelectric performance material are the simultaneous presence of flat bands (small dispersion) for large Seebeck coefficient and parabolic bands for the electron mobility (to increase the electrical conductivity). A schematic of the electronic DOS satisfying these criteria is depicted in Figure 8.1. These conditions in the band structure were found in a theoretical investigation of the thermoelectric properties of a La-filled skutterudite — $\text{La}(\text{Fe},\text{Co})_4\text{Sb}_{12}$.⁵⁵ The virtual crystal band structure of $\text{La}(\text{Fe}_{0.75}\text{Co}_{0.25})_3\text{Sb}_{12}$ and the calculated Hall concentration Hall number and thermopower at 600 K are shown in Figure 8.14 and Figure 8.15, respectively.⁵⁵ An abrupt increase in the carrier concentration is observed when the (p-doped) Fermi level is lowered to -26 mRy, corresponding to the onset of the flat-dispersive (heavy band) second electronic band near Γ .

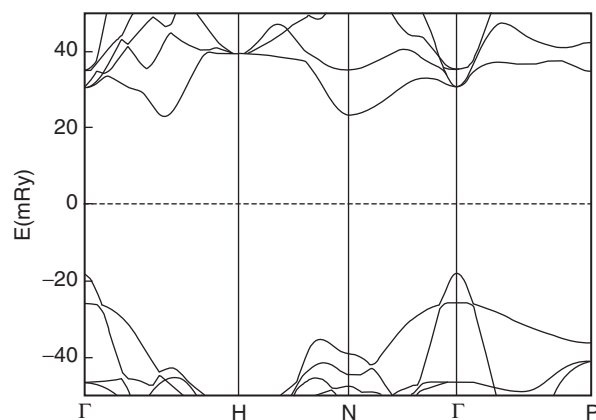


FIGURE 8.14 Calculated electronic band structure for a La-filled skutterudite, $\text{La}(\text{Fe}_{0.75}\text{Co}_{0.25})_3\text{Sb}_{12}$.

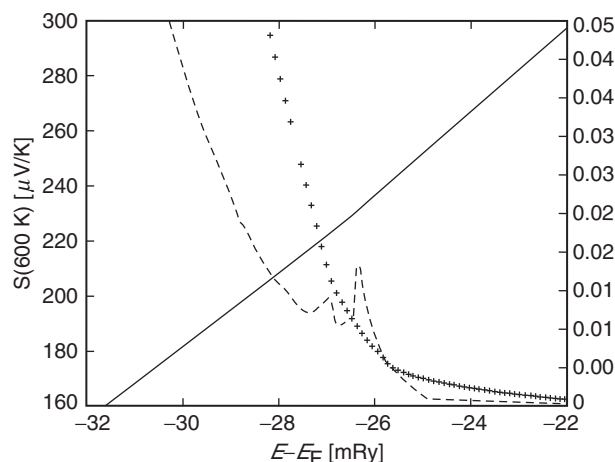


FIGURE 8.15 Calculated Seebeck coefficient and Hall concentration for $\text{La}(\text{Fe}_{0.75}\text{Co}_{0.25})_3\text{Sb}_{12}$.

Intuitively, one would expect the more complex the crystal structure the more complex the electronic band structure and more flexibility to manipulate the thermoelectric properties. A good example is the recently discovered low-temperature high-ZT CsBi_4Te_6 ⁵⁶ (see Figure 8.16 left panel). The band structure of CsBi_4Te_6 near the Fermi level is very complex and consists of both localized (weakly dispersive) and free-electron-like (highly dispersive) bands.⁵⁷ The integrand in Equation 8.12 in the calculation of the thermopower is approximately an even function weighted by the energy deviation from the Fermi energy ($E - E_F$). Therefore, if the DOS distribution of the filled and empty bands is symmetric at the Fermi energy, the net integrated value will be zero. In CsBi_4Te_6 , the DOS profile at the occupied band edge is very steep⁵⁷ (Figure 8.17). Within a rigid band approximation, the removal of a small amount of electrons (hole or p-doping) moves the Fermi level to lower energy and the DOS distribution around it becomes very asymmetric and consequently the magnitude of the integral becomes large. However, further reduction in the number of electrons creates a larger number of empty bands at energies higher than the Fermi level and reducing the magnitude of the integral. The dispersive bands are responsible for increasing the p-doped hole mobility and results in the high electrical conductivity. The thermal conductivity of CsBi_4Te_6 is anisotropic⁵⁶ (Figure 8.16). Importantly, the thermal conduction parallel to the crystal *b*-axis behaves like a normal crystalline solid, that is, the thermal conductivity increase with decreasing temperature but the thermal conductivity perpendicular to the *b*-axis is almost independent of temperature that typifies a glass-like behavior (Figure 8.16). The crystal structure of CsBi_4Te_6 may be described as Cs^+ intercalated between $[\text{Bi}_4\text{Te}_6]$ slabs as shown in the view down the *b*- and *c*-axes (Figure 8.18). The confinement between the layers restricts the motions of the Cs^+ vibrations in the directions perpendicular to the crystal *b*-axis. Therefore, Cs^+ ions act as “rattlers” and the localized vibrations strongly coupled with the framework via anticrossings of “localized” rattling vibrations into the acoustic branches of same symmetry. This results in resonant scatterings of thermal phonons and increases the thermal resistivity.

8.5 New Materials

8.5.1 Layered Cobalt Oxides

A new class of materials that has recently been attracting interest is the layered cobalt oxides. The layered cobalt oxide Na_xCoO_2 was reported to exhibit good thermoelectric performance by Terasaki et al.⁵⁸ who reported that single-crystal NaCo_2O_4 exhibits unusually large thermopower up to $100 \mu\text{V/K}$ at 300 K. There is also an unusually low resistivity of $200 \mu\Omega \text{ cm}$ in the direction parallel to the CoO_2 plane.

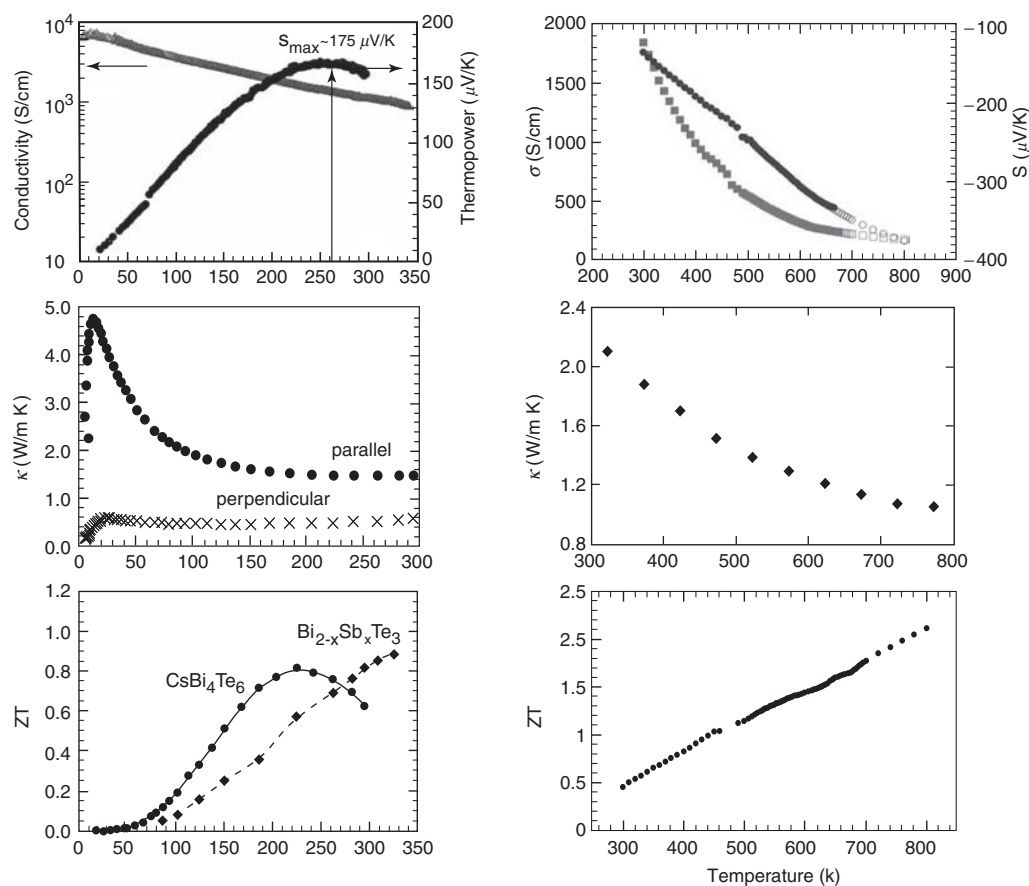


FIGURE 8.16 A comparison of the electrical conductivity, thermal conductivity, and figure-of-merit ZT for (left) CsBi_4Te_6 and (right) $\text{AgPb}_{18}\text{SbTe}_{20}$.

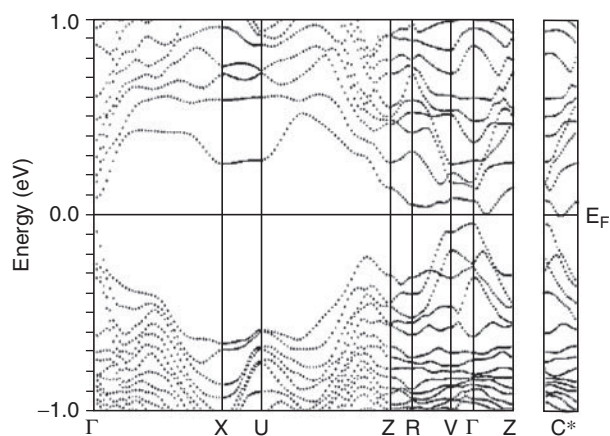


FIGURE 8.17 Calculated electronic band structure for CsBi_4Te_6 including the effects of spin-orbit coupling showing the complexity of the electronic bands near the Fermi level.

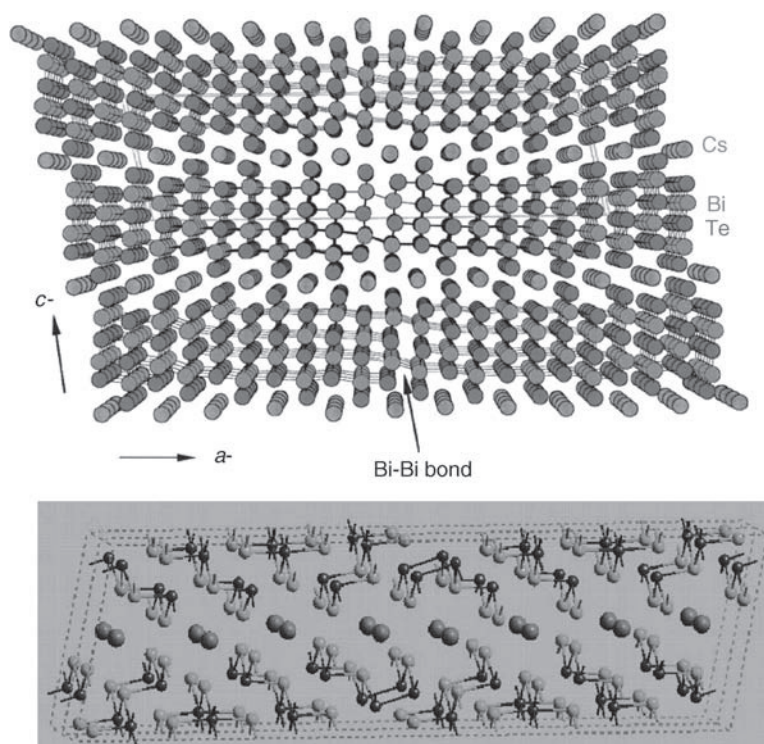


FIGURE 8.18 (See color insert following page 31-12.) Two perspective views of the crystal structure of CsBi_4Te_6 .

Fugita et al.⁵⁹ measured the thermal conductivity of a single-crystal NaCo_2O_4 and showed that ZT exceeded unity at 800 K. Another set of measurements on polycrystalline samples by Ohtaki et al.⁶⁰ suggested a fairly high $ZT \sim 0.8$. NaCo_2O_4 also has distinct advantages in that it exhibits high chemical stability at high temperature where most intermetallic compounds such as Bi_2Te_3 , CoSb_3 , and Si-Ge alloys cannot be used. These characteristics suggest that the doped Na_xCoO_2 compounds may have excellent potential for thermoelectric materials. In addition to their thermoelectric properties, these materials form novel two-dimensional superconductors⁶¹ since there is often a close connection between these two properties.

A unique property of NaCo_2O_4 is the relatively high carrier concentration in spite of the fact that it is an oxide. Terasaki et al.⁵⁸ found that the carrier density (n) of NaCo_2O_4 is of the order of $10^{21} - 10^{22} \text{ cm}^{-3}$, which is two orders of magnitude larger than that of conventional thermoelectric materials. Moreover, the high specific-heat coefficient ($40 - 50 \text{ mJ/mol K}^{-2}$)⁶² of $(\text{Na}, \text{Ca}) \text{Co}_2\text{O}_4$ and the finding that the temperature dependence of resistivity is proportional to T^p where p is 0.67 below 50 K and 1.2 above 80 K are indicative of a moderately strong electron-correlated system. It is possible that strong electron-electron correlations play an important role in the enhancement of the thermopower. Wang et al.⁶³ recently showed that $\text{Na}_{1+x}\text{Co}_2\text{O}_4$ is consistent with the behavior of a strongly correlated system in which the spin entropy accounts for almost all of the thermopower at 2 K and is a dominant fraction at 300 K. Thermopower measurements⁶⁴ of $\text{Na}_{1-x}\text{CoO}_2$ under pressures up to 20 GPa by Rivadulla et al. also demonstrated the importance of asymmetry in the DOS close to Fermi energy. In a correlated system, one expects that a conductor of low carrier concentration will have a large S because the diffusive part of S is the transport entropy, of the order of $k_B T/E_F$, where E_F is the Fermi energy. Since the primary role of Na is to donate charge to the CoO_2 framework and adjust the valance state of the Co ions, it may be possible to improve the thermoelectric properties by decreasing the carrier concentrations via different levels of Na doping. Koshibae et al.⁶⁵ proposed that, from strong interactions involving

spin configurations together with a generalized Heikes formula, the concentration of Na which determines the concentration ratio between Co^{3+} and Co^{4+} would be important for the enhancement of the Seebeck coefficient. The generalized Heikes formula was obtained from an analysis of the thermopower contribution in the Hubbard model.⁶⁶ The resulting expression for the thermopower is

$$Q = -\frac{k_b}{e} \ln\left(\frac{g_3}{g_4} \frac{x}{1-x}\right) \quad (8.16)$$

where k_b is the Boltzmann constant, e the electronic charge, g_3 and g_4 are the number of ways of arranging Co^{+3} and Co^{+4} sites in the crystal, respectively, and $x(= M/N_A)$ is the concentration of Co^{+4} ions. M is the number of Co^{+4} sites and N_A is the system size.

Experimental evidence for this possibility of large degeneracies in the Co^{3+} and Co^{4+} sites and the resulting spin-entropy from the disordered sites would actually dominate the thermopower in this transition-metal oxide. An interesting observation is that in a single crystal of $\text{Na}_{1.36}\text{Co}_2\text{O}_4$ even though the thermopower is very similar to NaCo_2O_4 , the in-plane resistivity (Ref. [63], Figure 1) is five orders of magnitude larger than that of NaCo_2O_4 (Ref. [58], Figure 2a).

The electronic band structure and thermopower of NaCo_2O_4 have been obtained from a simple theoretical transport model and a local density approximation calculation that employed the virtual crystal approximation (VCA)⁶⁷ and assumed that the effective electron scattering time has no energy dependence. An objective was to mimic the effects of fractional Na occupancy. A value of $S = 110 \mu\text{V/K}$ at 300 K was predicted although the effects of electron correlation were not included. This was in good agreement with the observed values of $100 \mu\text{V/K}$. Spin-polarized local spin-density approximation calculations were also performed in order to address the possibility of magnetic ordering. It was suggested that the most probable ground state of NaCo_2O_4 is ferromagnetically ordered. However, the most recent experimental susceptibility measurements show that $\text{Na}_{0.75}\text{CoO}_2$ ($\Theta = 166.4 \text{ K}$) and $\text{Na}_{1.36}\text{Co}_2\text{O}_4$ ($\Theta = 50 \pm 5 \text{ K}$)⁶³ are all antiferromagnetically ordered.

The validity of the rigid band and virtual crystal models have been tested for this material. Full potential linearized augmented plane-wave method (FPLAW) was used for calculations of the electronic band structure and the Seebeck and Hall coefficients.⁶⁸ For the VCA, Na atoms were replaced by a pseudoatom with fractional nuclear charge. The VCA approach therefore allows a self-consistent treatment of the change in the charge densities and carrier densities in electronic structure calculations. A comparison of the conduction bands derived from the VCA and rigid band calculations corresponding to stoichiometry NaCo_2O_4 is shown in Figure 8.19. It is evident that Co-dominated bands crossing the Fermi surface are very similar. There are, however, some minor but subtle differences. To calculate the transport integrals, Fermi surface integration was carried out with a very dense k -point mesh consisting of $\sim 40,000$ K points with the modified SKW band interpolation scheme.¹⁴ The calculated temperature dependence of the Seebeck coefficient as a function of the energy shift, $E - E_F$, to model the Na n-doping effect are plotted in Figure 8.20. The VCA and the rigid band model gave broadly similar results — both in the temperature dependence of the Seebeck coefficient and the doping effects on the Hall concentration. There were, however, discrepancies in the Hall coefficient when the energy shift is small and for the Seebeck coefficient at low temperature and at high doping levels (e.g., $x = 0.4$). These differences can be attributed to the subtle differences between the curvatures of several electronic bands close to the Fermi level, most noticeably along the $\Gamma \rightarrow K \rightarrow M$ direction. The results showed that both the rigid band model and VCA gave reasonable and almost equivalent results for the Seebeck and Hall coefficient. Also, the results showed that the numerical interpolation scheme proposed earlier to treat flat bands is reliable. The LDA + U calculations⁶⁹ were also performed but did not yield significant improvement, except for a slightly better agreement with experiment along $\Gamma-K$.

Based on the tight binding Hamiltonian, W. Koshibae et al.⁷⁰ suggested that the electronic structures can be described by Kagomé lattice hidden in the CoO_2 layer in Na_xCoO_2 . They presented a tight bonding band dispersion relation that captures the basic features of a first-principles band structure. The essence of their method is that the 3d electron hopping is via the oxygen atoms, indicating significant chemical

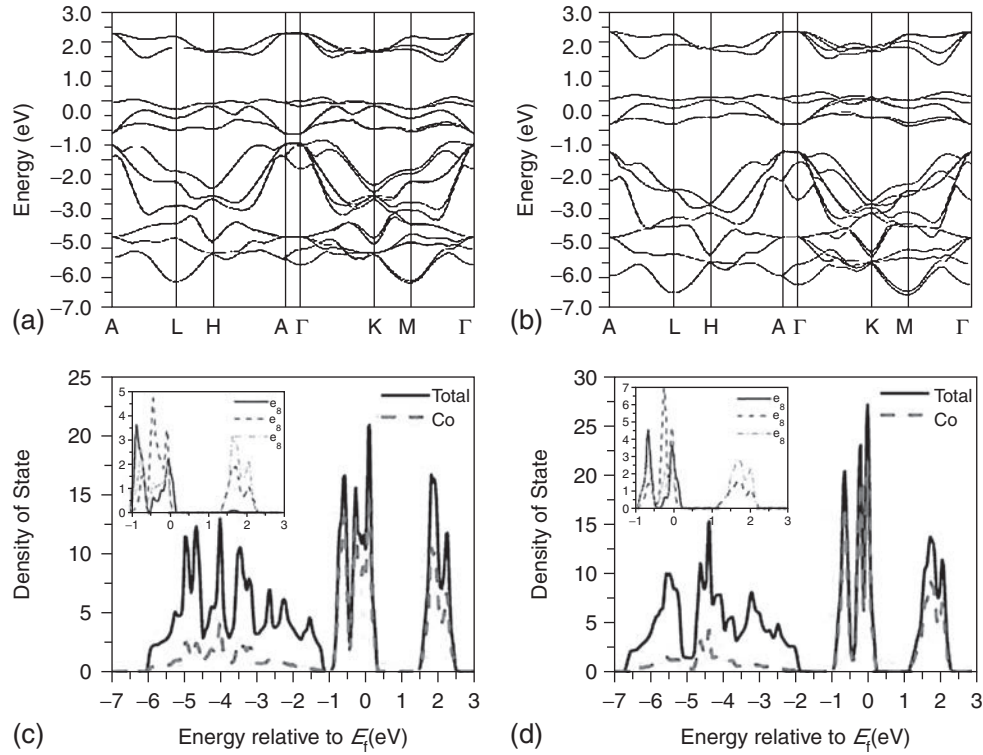


FIGURE 8.19 Calculated band structure and density of states (DOS) of NaCo_2O_4 . The left panel (a) and (c) calculated with the virtual crystal approximation and the right panel (b) and (d) with the rigid band model. The dotted curves in the DOS (c) and (d) are the projection of the Co d character in the linear augmented plane-wave spheres used in the calculations. The inset shows the Co d partial DOS.

interactions between Co and the oxygen atoms. Mulliken populations were analyzed by using *ab initio* pseudopotential density functional method employing linear combination of numerical atomic orbitals, SIESTA.⁷¹ This analysis confirmed that there exists a strong overlap between Co and O, in support of the argument of Koshibae et al.

The recent report indicating that there may be an additional spin entropy contribution to the thermoelectric efficiencies of a material has been further tested. The effects of spin polarization on the electronic structure of $\text{Na}_{1+x}\text{Co}_2\text{O}_4$ was examined with spin-polarized calculations. The electronic states were constrained to ferromagnetic ordering. For a low spin state, if the crystal is restricted to charge neutrality, there can be no spin-unpaired electrons within the rigid band model. This is because, since $\text{Na}_2\text{Co}_2\text{O}_4$ was taken as the model, all the Co atoms will be in the Co^{3+} valence state and the rigid band model is not applicable. On the other hand, with the VCA, since half occupied Na ion sites in the NaCo_2O_4 crystal were adopted there must be an equal concentration of Co^{3+} and Co^{4+} to satisfy the neutrality condition. Spin-polarized calculations on the ferromagnetic state were consistent with this simple analysis. The ferromagnetic band structure for half-occupied Na ion sites calculated with the VCA is shown in Figure 8.21. When compared to the nonspin-polarized result, the ferromagnetic state was energetically more favorable although the total energy difference is only 79 meV per unit cell. Inspection of the α - and β -spin DOS indicates that NaCo_2O_4 is a half-metal with a spin moment of $1 \mu_B$ per unit cell. In each unit cell there is one spin-unpaired Co d electron. In this case, Co^{3+} has a t_{2g}^6 low spin configuration. The $1 \mu_B$ per unit cell shows that Co^{4+} takes its low spin ($S = 1/2$) state and has a t_{2g}^5 configuration, i.e., a “hole” in the t_{2g} orbital giving a net magnetic moment of $1 \mu_B$.

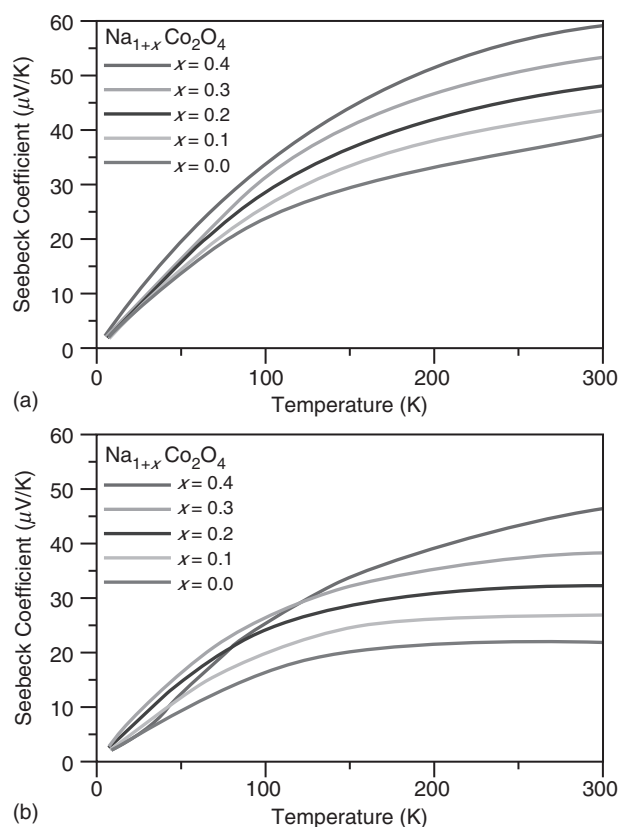


FIGURE 8.20 (See color insert following page 31-12.) The calculated thermopower vs. temperature at different doping levels for (a) the virtual crystal approximation and (b) the rigid band model.

Results of calculations for other fractional Na ion site occupancies with spin polarization are listed in Table 8.1. The Na concentration has a significant effect on the total spin contribution to the magnetic moment of the Co atoms. The results show that higher Na concentrations result in a higher tendency for the Co *d* electrons to be spin-paired. The generalized Heikes formula⁷² for a strong interaction case involving spin configuration (Equation 8.16) was employed. For a low spin state, $g_3 = 1$, and $g_4 = 6$. Within this approximation, the Seebeck coefficient is mainly determined by the value of x . In the model proposed in Ref. [63], the spin-entropy contribution depends mainly on the so-called “free” spins, which are not antiferromagnetically ordered at low temperature ($T \ll \Theta$, where Θ is the Neel temperature). This indicates that the Na concentration will determine the spin entropy contribution to the Seebeck coefficient. We have not studied the antiferromagnetic state of $\text{Na}_{1+x}\text{Co}_2\text{O}_4$ here. A proper study would require the construction of a larger supercell to account for the antiferromagnetic order for different Na concentrations. The calculation would become more complicated as it would involve full geometry optimization in addition to the computation of the band structure. Such a study will be reported in the future. From the results of spin-polarized band structure calculations, the magnetic moment is apparently strongly dependent on the Na ion occupancy. For example, in the limit when there are no Na atoms, all the Co atoms would be in the high spin Co^{4+} valance state. In this case, there would be no spin exchange and the spin entropy contribution will be zero. In the other limit, if the Na sites were fully occupied as in the α phase (NaCoO_2), there would be no net magnetic moment and the spin-entropy contribution would diminish. This suggestion, however, is in apparent contradiction with a recent experimental study which showed that the α phase has an even higher Seebeck coefficient. Obviously, more detailed experimental and theoretical studies are needed in order to explain this novel phenomenon.

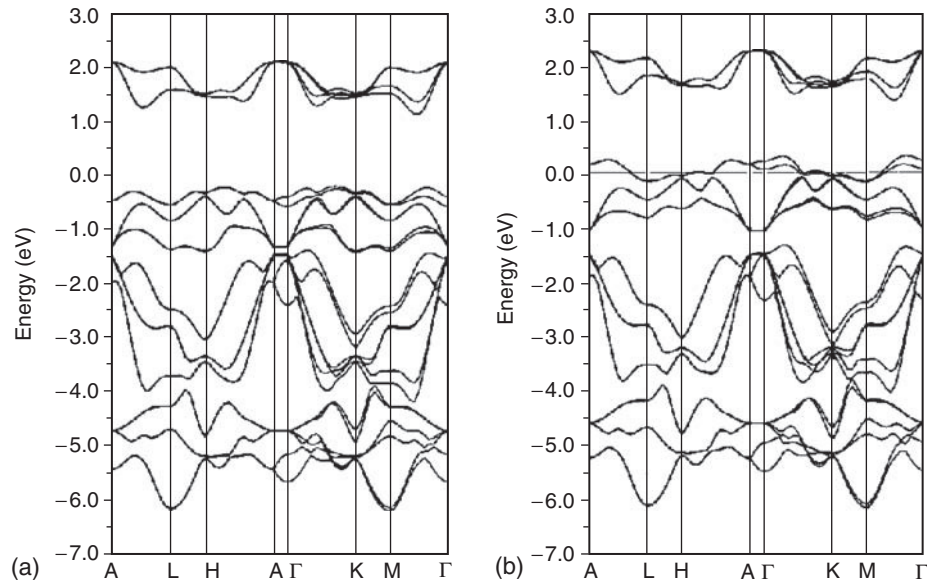


FIGURE 8.21 The ferromagnetic band structure of NaCo_2O_4 : (a) up-spin, (b) down-spin.

The rigid band approximation compared well with the VCA for Na cobalt oxides. However, in a critical testing of the calculated band structures, Seebeck and Hall coefficients showed that the simple band structure model in the paramagnetic state, either using the rigid band model or VCA, was not completely appropriate. It was interesting, however, that even without the consideration of the spin entropy, a paramagnetic ground state would yield a high Seebeck coefficient comparable to the experimental observation. Perhaps therefore, optimization of the Na concentration together with the spin-entropy contribution may yield higher thermopower.

A very recent study⁷³ using the Boltzmann transport equation for the electronic structure (determined from photoemission experiments) suggested that the unique electronic structure of the layered cobalt oxides was solely responsible for both the large thermoelectric power and metallic conductivity. The desirable low thermal conductivity that is also required for a large thermoelectric power is attributed to the misfit structure between the CoO_2 layers and other layers in the $\text{Na}_x\text{Co}-\text{O}_2$ material.⁷⁴ Clearly more research, both experimental and theoretical, is required to completely characterize and understand this promising material.

8.5.2 Quantum Wells and Quantum Wires

The apparent limitations for increasing the thermoelectric performance in three-dimensional materials can, in principle, be overcome in lower-dimensional solids. Theoretical studies such as

TABLE 8.1 Ferromagnetic Solution for $\text{Na}_{1+x}\text{Co}_2\text{O}_4$ with Different x , the Magnetic Moment per Unit Cell, and the Total Energy Difference Relative to the Paramagnetic Electronic State

x	Magnetic Moment per Unit Cell (μ_B)	Energy (meV/Unit Cell)
0	1.0	-79.2
0.1	0.9	-67.0
0.2	0.8	-55.3
0.3	0.7	-42.1
0.4	0.6	-30.3

those of Hicks and Dresselhaus^{75–77} suggested that ZT could be significantly increased in low-dimensional quantum wells and superlattices due to the increase in electronic DOS per unit volume. For quantum wires having infinite potentials, one could achieve even greater densities of states and therefore higher values of ZT . This work has been summarized in an excellent review⁷⁸ in this series. Subsequent work on three-dimensional superlattice systems⁷⁹ using a variety of methods including three-dimensional band structure calculations found that ZT was limited at all widths for a quantum well. More recent work employing a full electronic superlattice band structure calculation together with a multisubband Boltzmann equation approach for electron or hole-phonon scattering⁸⁰ obtained the result that relaxation of the constant relaxation time approximation would yield a much lower value of the power factor $S^2\sigma$ than in the case of constant relaxation time. It was suggested that free-standing quantum wires could be a way to overcome this limitation since heat transport could be minimized.

In a more recent report,⁸¹ an analysis of the thermoelectric properties of superlattice nanowires based on the Boltzmann transport equations for one-dimensional systems was presented. Using the Kronig–Penney model for calculation of the electronic DOS and using the constant relaxation time approximation, it was shown that the ZT was calculated to be strongly dependent on the segment lengths of components in the quantum wire, the wire diameter, crystal orientation in the wire, selection of material constituents, the Fermi energy, and the segment length ratio. A schematic diagram of a superlattice nanowire used for the above reported calculations is shown in Figure 8.22. These parameters may play as an important role in the ultimate efficiency of these materials as the relaxations times. With the optimization of these parameters, ZT of > 4 was predicted for these simple and idealized models. It is clear that much theoretical and experimental work needs to be done to define the limits of the thermoelectric efficiencies of quantum wells and nanowire superlattices.

8.5.3 Complex Chalcogenides

A very recent report indicates that a family of complex chalcogenide compounds, $\text{AgPb}_m\text{SbTe}_{2+m}$, exhibit large ZT values⁸². These compounds were originally prepared assuming statistical disorder of the Ag, Pb, and Sb atoms on Na sites in a NaCl structure ($Fm\bar{3}m$ symmetry, Figure 8.23). The recent study showed that there is, however, evidence of order in these materials. The temperature dependence of the electrical and thermal conductivities, Seebeck coefficient, and ZT reported for $\text{AgPb}_{18}\text{SbTe}_2$ is compared with another promising high efficiency thermoelectric material, CsBi_4Te_6 , in Figure 8.16. The electrical conductivity decreases with temperature as in a normal metal. Furthermore, the thermal conductivity does not show glass-like anomaly and decreases fairly slowly from 300 to 800 K. These materials do not show the feature of a glass and, therefore, probably should not be considered as members of the class of phonon glasses where there is significant lowering of the thermal conductivity at low temperature. The very high ZT is the result of a complicated balance of the Seebeck coefficient, electrical and thermal conductivity. The complexity of the crystal structure which provides a large number of

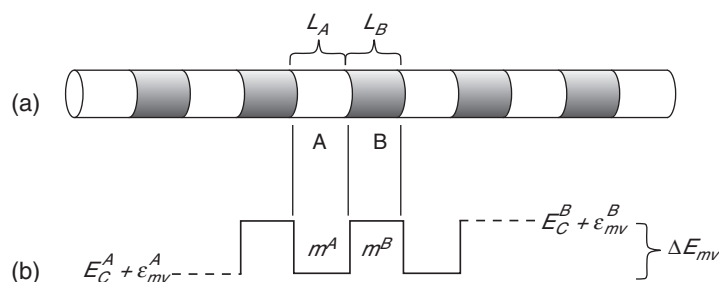


FIGURE 8.22 (a) Schematic diagram for a model superlattice nanowire and (b) the potential profile of a conduction subband in a superlattice nanowire from Ref. [81].

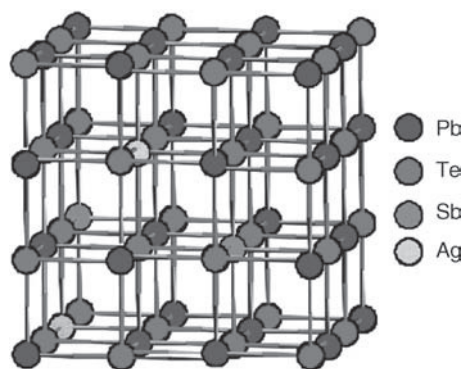


FIGURE 8.23 (See color insert following page 31-12.) The unit cell for a disordered complex chalcogenide.

degrees of freedom means that the critical components, thermal conductivity, electrical conductivity, and Seebeck coefficient can be easily modified for the optimization of ZT .

Although the exact origin of the high ZT of ~ 2.2 at 800 K is not yet determined, interesting suggestions based on *ab initio* electronic structure calculations⁸³ using the full potential density-functional method as implemented in the WIEN2K code¹⁶ were reported and analyzed to suggest that the high ZT values could originate from differing ordering arrangements of Ag–Sb atoms in the $\text{AgPb}_m\text{SbTe}_{2+m}$ materials. Typical models for the unit cells of these compounds are shown in Figure 8.24. The electronic DOS near the bandgap compared to that of pure PbTe was calculated to be very sensitive to these ordering arrangements leading to the appearance of distinct resonant states. These resonant states are suggested to be related to the high figure-of-merit in this material. These resonant states are effectively arising from the presence of “nanodots” in the cubic lattices.

8.6 Concluding Remarks

The advances in theoretical methods summarized in this review have now led to improvement in the efficient design of materials. *Ab initio* methods enable the researcher to predict material properties often with “experimental” accuracy. These methods require only the constituent atoms and their approximate crystal structures. The recently developed techniques for data-mining aided with accurate quantum mechanical calculations^{84,85} promise to have a significant role in the design of new materials. These methods could be particularly useful for the development of new and more efficient thermoelectric materials. Many of the steps in experimental testing of materials could, in principle, be reduced or

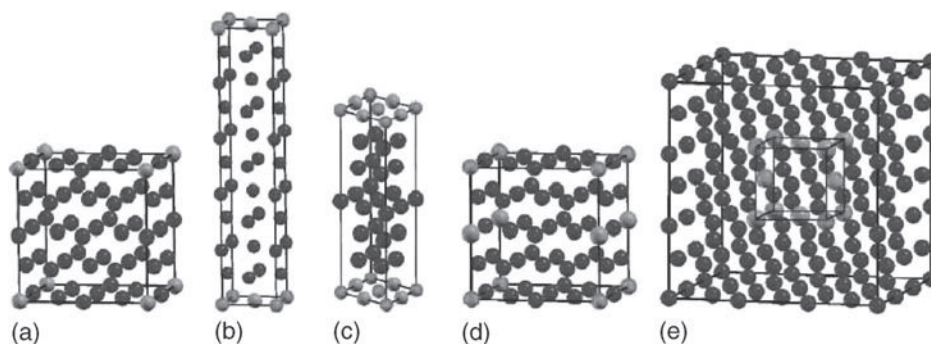


FIGURE 8.24 (See color insert following page 31-12.) Suggested unit cell models for the $\text{AgPb}_m\text{SbTe}_{2+m}$ material used in the theoretical calculations. Only the Pb FCC lattice atoms are shown with Pb atoms blue, Ag red, and Sb green.

eliminated. The rapid improvement in computational hardware and software and the reliability of the calculated results will almost certainly ensure a major or dominant role for theory in the design of new materials. The simple one-band model is no longer adequate for the prediction of the thermopower of complex materials. It is necessary to consider and manipulate two types of electronic bands — a nondispersive band for the enhancement of Seebeck coefficient and a dispersive band for electron transport. In combination with the paradigm of phonon glass electron crystal, new high efficiency thermoelectric materials may be discovered or designed.

References

1. Mahan, G.D. and Sofo, J.O., *Proc. Natl Acad. Sci. USA*, 93, 7436, 1996.
2. Singh, D.J., Theoretical and computational approaches for identifying and optimizing novel thermoelectric materials, *Semicond. Semimetals*, 70, 125, 2001.
3. For example see a recent book by Martin, R.M., *Electronic Structure: Basic Theory and Practical Methods*, Cambridge University Press, Cambridge, UK, 2004.
4. Hohenberg, P. and Kohn, W., *Phys. Rev.*, 136, 864, 1964.
5. Sham, L.J. and Kohn, W., *Phys. Rev.*, 145, 561, 1966.
6. Parr, R.G. and Wang, W., *Density Functional Theory of Atoms and Molecules*, Oxford University Press, New York 1989.
7. Perdew, J.P. and Wang, W., *Phys. Rev. B*, 33, 8800, 1986.
8. Lee, C., Yang, W., and Parr, R.G., *Phys. Rev. B*, 37, 785, 1988.
9. Singh, D.J., *Plane-waves, Pseudopotentials, and the LAPW Method*, Kluwer Academic, Boston, 1994.
10. Dreyse, H., *Electronic Structure and Physical Properties of Solids: The Uses of the LMTO Method*, Lecture Notes in Physics, Vol. 535. Springer, Berlin, 2000.
11. Altmann, S.L., *Band Theory of Solids: An Introduction from the Point of View of Symmetry*, Clarendon Press, Oxford, 1994.
12. Ziman, J.M., *Principles of the Theory of Solids*, Cambridge University Press, Cambridge, UK, 1964.
13. Kim, S.-G., Mazin, I.I., and Singh, D.J., *Phys. Rev. B*, 57, 6199, 1998.
14. Uehara, K. and Tse, J.S., *Phys. Rev. B*, 61, 1639, 2000.
15. Scheidmantel, T.J., Ambrosch-Draxl, C., Thonhauser, T., Badding, J.V., and Sofo, J.O., *Phys. Rev. B*, 68, 125210, 2003.
16. Blaha, P., Schwarz, K., Madsen, G.K.H., Kvasnika, D., and Luitz, J., In *Wien2k, An Augmented Plane-Wave — Local Orbitals Program for Calculating Crystal Properties*, K. Schwarz, ed. Techn. Universität Wien, Austria, 2001.
17. Xing, G., Klug, D.D., and Tse, J.S., *J. Phys. Condens. Matter*, 16, 6493, 2004.
18. Slack, G.A., In *CRC Handbook of Thermoelectrics*, D.M. Rowe, ed., p. 407. CRC Press, Boca Raton, FL, 1995.
19. Cahill, D.G. and Pohl, R.O., *Ann. Rev. Phys. Chem.*, 39, 93–121, 1988.
20. Myles, C.W., Dong, J., and Sankey, O.F., *Phys. Rev. B*, 64, 165202, 2001, and references therein.
21. Nola G.S. and Slack, G.A., *American Scientist*, 89, 136, 2001; Tse, J.S. and Li, Z.Q., *Trends Chem. Phys.*, 9, 91, 2001.
22. Davidson, D.W. 1973. In *Water: A Comprehensive Treatise*, F. Franks, ed. Plenum Press, New York.
23. Adams, G.B., Keeffe, M.O., Demkov, A.A., Sankey, O.F., and Huang, Y.M., *Phys. Rev. B*, 49, 8048, 1994; Demkov, A.A., Sankey, O.F., Schmidt, K.E., Adams, G.B., and Keeffe, M.O., *Phys. Rev. B*, 50, 17001, 1994; Saito, S and Oshiyama, A., *Phys. Rev. B*, 51, 2628, 1995.
24. Moriguchi, K., Shintani, M.Y.A., and Yamanaka, S., *Phys. Rev. B*, 61, 9859, 2000.
25. Ramachandra, G., et al., *Phys. Rev. B*, 61, 12294, 1999.
26. Dong, J., Sankey, O.F., and Kern, G., *Phys. Rev. B*, 60, 950, 1999.
27. Tse, J.S., *J. Incl. Phenom.*, 17, 259, 1994.

28. Tse, J.S., Li, Z., and Uehara, K., *Europhys. Lett.*, 56, 261, 2001.
29. Tse, J.S., Ratcliffe, C.I., Powell, B.M., Sears, V.F., and Handa, Y.P., *J. Phys. Chem. A*, 101, 4491, 1997.
30. Cohn, J.L., Nolas, G.S., Fessatidis, V., Metcalf, T.H., and Slack, G.A., *Phys. Rev. Lett.*, 82, 779, 1999.
31. Li, Z.Q., Uehara, K., and Tse, J.S., *Europhys. Lett.*, 56, 275, 2001.
32. Baumert, J., Gutt, C., Shpakov, V.P., Tse, J.S., Krisch, M., Müller, Requardt, H., Klug, D.D., Janssen, S., and Press, W., *Phys. Rev. B*, 68, 174301, 2003.
33. Tse, J.S. and White, M.A., *J. Phys. Chem.*, 92, 5006, 1988.
34. Baumert, J., Gutt, C., Shpakov, V.P., Tse, J.S., Krisch, M., Müller, M., Requardt, H., Klug, D.D., Janssen, S., and Press, W., *Phys. Rev. B*, 68, 174301, 2003.
35. Kasper, J.S., Hagenmuller, P., Pouchard, M., and Cros, C., *Science*, 150, 1713, 1965.
36. Lee, S., Rousseau, R., and Wells, C., *Phys. Rev. B*, 46, 12121–12131, 1992; Lee, S., *Ann. Rev. Phys. Chem.*, 47, 397, 1996.
37. For the tight-binding analysis, each Si atom is described by single exponent 3s and 3p Slater orbitals, the exponents of which were carefully chosen to match atomic wave functions as obtained from an atomic local density approximation calculation. A mesh of at least 1000 *k*-points over the symmetry-inequivalent portion of the BZ was used to ensure convergence of moments and energies.
38. Adams, G.B., Keeffe, M.O., Demkov, A.A., Sankey, O.F., and Huang, Y.M., *Phys. Rev. B*, 49, 8048, 1994; Demkov, A.A., Sankey, O.F., Schmidt, K.E., Adams, G.B., and Keeffe, M.O., *Phys. Rev. B*, 50, 17001, 1994.
39. Ker, A., Todorov, E., Rousseau, R., Uehara, K., Lannuzel, F.-X., and Tse, J.S., *Chem. Eur. J.*, 8, 2787, 2002.
40. Tse, J.S., Uehara, K., Rousseau, R., Ker, A., Ratcliffe, C.I., White, M.A., and MacKay, G., *Phys. Rev. Lett.*, 85, 114, 2000.
41. Nolas, G.S., Ward, J.M., Gryko, J., Qiu, L., and White, M.A., *Phys. Rev. B*, 64, 153201, 2001.
42. Freeman, J.J. and Anderson, A.C., *Phys. Rev. B*, 34, 5684–5690, 1986.
43. Nolas, G.S., Cohn, J.L., Slack, G.A., Schujman, S.B., *Appl. Phys. Lett.*, 73, 178, 1998.
44. Cros, C., Pouchard, M., and Hagenmuller, J., *J. Solid State Chem.*, 2, 570, 1970.
45. Mott, N.F., *J. Solid State Chem.*, 6, 348, 1973.
46. As noted in Kawaji, H., et al., *Phys. Rev. Lett.*, 74, 1427, 1995, even with well-compacted powder samples of apparently similar composition, the measured Seebeck coefficient can differ by a significant factor. We tested the computational procedure against a well characterized single crystal of b-Zn₄Sb₃. The calculated Seebeck coefficients were in very good agreement with experiment and also with a previous LAPW study (Kim, S., et al., *Phys. Rev. B*, 57, 6199, 1998).
47. Blake, N.P., Mollnitz, L., Kresse, G., and Metiu, H., *J. Chem. Phys.*, 111, 3133, 1999.
48. Uher, C., In *Chemistry, Physics, and Materials Science of Thermoelectric Materials: Beyond Bismuth Telluride*, M.G. Kanatzidis, T.P. Hogan and S.D. Mahanti, eds., p. 121. Kluwer Academic/Plenum, Dordrecht/New York, 2003.
49. Nolas, G.S., Morelli, D.T., and Tritt, T.M., *Ann. Rev. Matter Sci.*, 29, 89, 1999.
50. Sales, B.C., Mandrus, D., Chakoumakos, B.C., Keppens, V., and Thomson, J.R., *Phys. Rev. B*, 56, 15081, 1997, see also Hermanm, R.P., Jin, R., Schweika, W., Grandjean F., Mandrus, D., Sales, B.C., and Long, G.J., *Phys. Rev. Lett.*, 90, 135505, 2003; Keppens, V., Mandrus, D., Sales, B.C., Chakoumakos, B.C., Dai, P., Coldea, R., Maple, M.B., Gajewski, D.A., Freeman, E.J., *Nature*, 395, 876, 1998.
51. Feldman, J.L., Singh, D.J., Mazin, I.I., Mandrus, D., and Sales, B.C., *Phys. Rev. B*, 61, 9209, 2000; Feldman, J.L., Singh, D.J., Kendziora, C., Mandrus, D., and Sales, B.C., *Phys. Rev. B*, 68, 94301, 2003.
52. Berardan, D., Alleno, E., Rouleau, O., Godart, C., Puyet, M., Lenoir, B., Scherrer, H., Girard, L., Ravot, D., *Proceedings of Eighth European Workshop on Thermoelectrics of ETS — Poland*, Sept 15–17, 2004.

53. Kurmaev, E.Z., Moewes, A., Shein, I.R., Finkelstein, L.D., Ivanovskii, A.L., and Anno, H., *J. Phys. Condens. Matter*, 16, 979, 2004.
54. Mott, N.F., and Jones, H., *The Theory of the Properties of Metals and Alloys*, Dover Publications, New York, 1958.
55. Singh, D.J. and Mazin, I.I., *Phys. Rev. B*, 56, R1650–R1653, 1997.
56. Chung, D.Y., Hogan, T., Brazis, P., Rocci-Lane, M., Kannewurf, C., Bastea, M., Uher, C., Kanatzidis, M.G., *Science*, 287, 1024, 2000.
57. Larson, P., Mahanti, S.D., Chung, D.Y., and Kanatzadis, M.G., *Phys. Rev. B*, 65, 45205, 2002.
58. Terasaki, I., Sasago, Y., and Uchinokura, K., *Phys. Rev. B*, 56, R12685, 1997.
59. Fujita, K., Mochida, T., and Nakamura, K., *Jpn. J. Appl. Phys.*, 40, 4644, 2001.
60. Ohtaki, M., Nojiri, Y., and Maeda, E., *Proceedings of the 19th International Conference on Thermoelectrics 2000*, D.M. Rowe, ed., p. 190. Babrow, Wales, 2000.
61. Takada, K., Sakurai, H., Takayama-Muromachi, E., Izumi, F., Dilanian, R.A., and Sasaki, T., *Nature*, 422, 53–55, 2003.
62. Ando, Y., Miyamoto, N., Segawa, K., Kawata, T., and Terasaki, I., *Phys. Rev. B*, 60, 10584, 1999.
63. Wang, Y., Rogado, N.S., Cava, R.J., and Ong, N.P., *Nature*, 423, 425, 2003.
64. Rivadulla, F., Zhou, J.S., and Goodenough, J.B., *Phys. Rev. B*, 68, 075108, 2003.
65. Koshibae, W., Tsutsui, K., and Maekawa, S., *Phys. Rev. B*, 62, 6869, 2000.
66. Chaikin, P.M. and Beni, G., *Phys. Rev. B*, 13, 647, 1976.
67. Singh, D.J., *Phys. Rev. B*, 61, 13397, 2000.
68. Gao, X., Tse, J.S., and Klug, D.D., *J. Phys. Condens. Matter*, 16, 6493, 2004.
69. Anisimov, V.I., Solov'yev, I.V., Korotin, M.A., Czyżyk, M.T., and Sawatzky, G.A., *Phys. Rev. B*, 48, 16929, 1993.
70. Koshibae, W. and Maekawa, S., *Phys. Rev. Lett.*, 91, 257003, 2003.
71. Ordejón, P., Artacho, E., and Soler, J.M., *Phys. Rev. B*, 53, 10441, 1996.
72. Koshibae, W., Tsutsui, K., and Maekawa, S., *Phys. Rev. B*, 62, 6869, 2000.
73. Takeuchi, T., Konda, T., Takami, T., Takahashi, H., Ikuta, H., Mizutani, U., Soda, K., Funahashi, R., Shikano, M., Mikami, M., Tsuda, S., Yokoya, T., Muro, S.T., *Phys. Rev. B*, 69, 125410, 2004.
74. Miyazaki, Y., Onoda, M., Oku, T., Kikuchi, M., Ishii, Y., Ono, Y., Morii, Y., and Kajitani, T., *J. Phys. Soc. Jpn.*, 71, 495, 2002.
75. Hicks, L.D. and Dresselhaus, M.S., *Phys. Rev. B*, 47, 12727, 1997.
76. Hicks, L.D. and Dresselhaus, M.S., *Phys. Rev. B*, 47, 16631, 1997.
77. Hicks, L.D., Harman, T.C., and Dresselhaus, M.S., *Appl. Phys. Lett.*, 63, 3230, 1993.
78. Dresselhaus, M.S., Lin, Y.-M., Cronin, S.B., Rabin, O., Black, M.R., and Dresselhaus, G., In *Semiconductors and Semimetals*, Vol. 71, T.M. Tritt, ed. Academic Press, New York, 2001.
79. Broido, D.A., Reinecke, T.L., In *Semiconductors and Semimetals*, Vol. 71, T.M. Tritt, ed. Academic Press, New York, 2001.
80. Broido, D.A. and Reinecke, T.L., *Phys. Rev. B*, 64, 045324, 2001.
81. Lin, Y.-M. and Dresselhaus, M.S., *Phys. Rev. B*, 68, 075304, 2003.
82. Hsu, K.F., Loo, S., Guo, F., Chen, W., Dyck, J.S., Uher, C., Hogan, T., Polychroniadis, E.K., and Kanatzidis, M.G., *Science*, 303, 818, 2003.
83. Bilc, D., Mahanti, S.D., Quarez, E., Hsu, K.-F., Pcionek, R., and Kanatzidis, M.G., *Phys. Rev. Lett.*, 93, 146403, 2004.
84. Curtarolo, S., Morgan, D., Persson, K., Rodgers, J., and Ceder, G., *Phys. Rev. Lett.*, 91, 135503, 2003.
85. Morgan, D., Rodgers, J., and Ceder, G., *J. Phys. Condens. Matter*, 15, 4361, 2003.

